

Imaging ^{55}Fe Electron Tracks in a GEM-based TPC Using a CCD Readout

N. S. Phan,^{1,2} E. R. Lee,³ D. Loomba

*Department of Physics and Astronomy, University of New Mexico,
210 Yale Blvd NE, Albuquerque, NM 87106, USA*

E-mail: nphan@unm.edu

ABSTRACT: Images of resolved 5.9 keV electron tracks produced from ^{55}Fe X-ray interactions, and the corresponding energy spectrum, are presented for the first time using an optical readout time projection chamber (TPC). These tracks were produced in low pressure carbon tetrafluoride (CF_4) gas, and imaged with a fast lens and low noise CCD camera system using the secondary scintillation produced in GEM/THGEM amplification devices. The GEM/THGEMs provided effective gas gains of $\gtrsim 2 \times 10^5$ in CF_4 at low pressures in the 25-100 Torr range. The ability to resolve such low energy particle tracks has important applications in dark matter and other rare event searches, as well as in X-ray polarimetry. A practical application of the optical signal from ^{55}Fe is that it provides a tool for mapping the detector gain spatial uniformity.

KEYWORDS: Optical TPC, ^{55}Fe electron tracks, GEMs, Thick GEMs, CF_4 , CCD camera

¹Corresponding author

²Present address: Los Alamos National Laboratory, Los Alamos, New Mexico 87545, U.S.A.

³Deceased

Contents

1	Introduction	1
2	Detector Setup	2
3	Detector Calibrations	4
3.1	GEM/THGEM Gain	4
3.2	CCD Calibration	6
4	Results	7
4.1	100 Torr	7
4.2	25, 35 & 50 Torr	8
4.3	Light Yield and Contaminants	11
5	Conclusion	13

1 Introduction

We show the first results from a high resolution, high signal-to-noise gas TPC used to optically detect and resolve 5.9 keV electron tracks. All measurements were taken at low pressures in the 25-100 Torr range, where low energy tracks are long enough to be resolved. The electron tracks produced by the photoabsorption of 5.9 keV ^{55}Fe X-rays were optically imaged and resolved using a low-noise, high quantum efficiency CCD (charge-coupled device) camera in conjunction with GEM (gas electron multiplier) amplification. Although this capability has been demonstrated using charge readouts (e.g., using pixels or strips) [1–4], the lowest energy tracks imaged with optical readouts have been in the 15-22 keV range [5–7].

Reconstructing low energy recoil tracks is important for a number of applications, such as directional dark matter [8] and X-ray polarization [1, 2] experiments, where information sought about the incident particle is contained in the properties of the particle tracks produced in the interaction. For directional dark matter experiments, the measured properties of the track are used for background discrimination [9, 10], and to search for the directionality signature imprinted on nuclear recoils resulting from galactic dark matter interactions [11, 12]. In X-ray polarimetry, the angular distribution of photoelectrons produced in the absorption of X-rays from astrophysical sources is used to determine their polarization [1–3]. Due to the nature of the sources for both applications, detecting and *resolving* tracks of electron and nuclear recoils down to the lowest energies, <10 keV, greatly improves the experimental sensitivity.

The stringent requirements for these applications have led to the low pressure gas TPC technology as the basis for most experimental efforts. The advent of Micro-Patterned Gas Detectors

(MPGDs) have enabled high gas gains with fine-grained charge or optical readouts, thereby providing the necessary segmentation to image short tracks. MPGDs with strip [4] or pixel [1–3] charge readouts have been used to successfully resolve electron tracks in 2D or 3D at or below ^{55}Fe energies. With optical readouts, a variety of methods have been applied to detect and image recoil tracks using the scintillation light produced in the avalanche region for certain gases. The simplest of these use a PMT, which measures the light intensity and, using the pulse shape, one component of the recoil track [13, 14]. To image 2D tracks, optical systems consisting of a CCD camera and some combination of lenses, image intensifiers and fiber optic plates have been used; e.g. [9, 15–18]. For example, with a capillary gas proportional counter coupled to an image intensified CCD through a lens system [7], 2D electron tracks have been optically resolved down to ~ 15 keV.

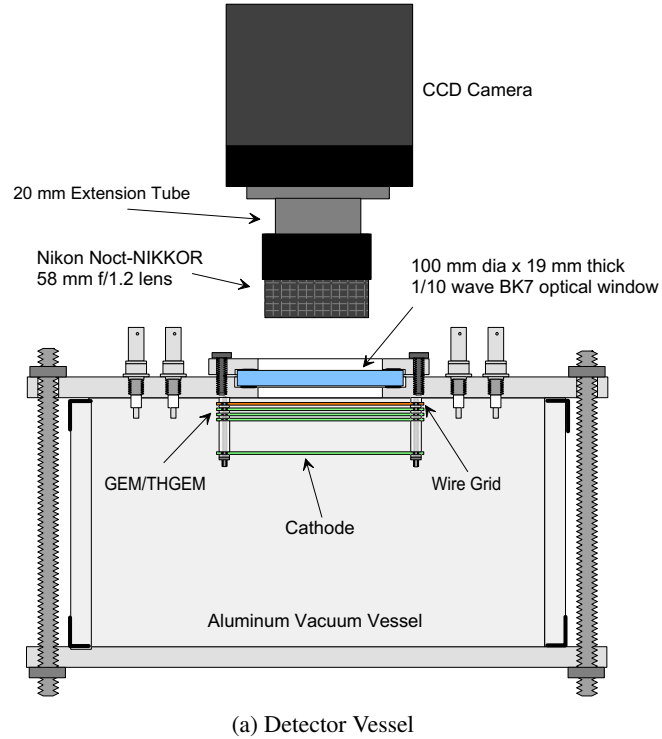
The detector used for our measurements was a TPC filled with high-purity CF_4 gas, with GEMs and thick GEMs (THGEMs) used to provide gas amplification and the scintillation light captured by a CCD-based optical readout system. GEMs are a micro-pattern amplification device invented by Sauli at CERN [19]; further information on the operation of GEMs with CCD readout can be found in Refs. [16, 18, 20, 21]. THGEMs are similar to GEMs but with dimensions (thickness, hole size, and pitch) that are typically ≥ 3 times larger. Exceptionally high gas gains have been achieved in both types of amplification devices, but THGEMs have been shown to excel down at the low pressures of interest here [22].

2 Detector Setup

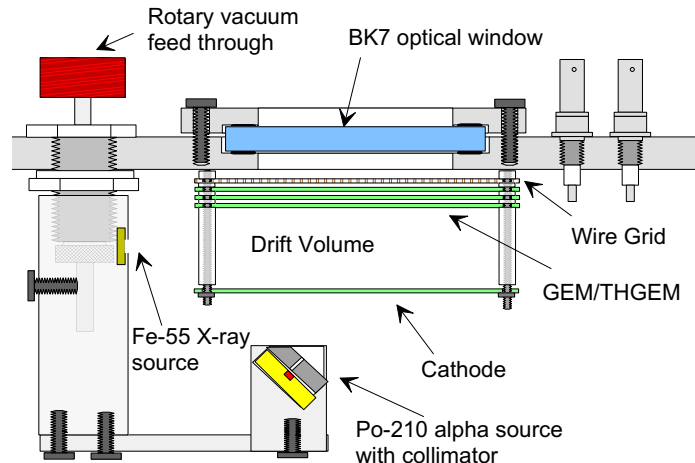
A schematic of the detector setup is shown in Figure 1. Measurements were made at four pressures, 25 Torr, 35 Torr, 50 Torr and 100 Torr. At each pressure, the choice of amplification device between single GEM/THGEM or multiple GEMs/THGEMs was made to maximize stability, gas gain, and spatial resolution. For the 100 Torr measurements, the detector used a cascade of three standard copper GEMs separated by 2 mm (Figure 1). The GEMs were manufactured at CERN using a 50 μm thick, $7 \times 7 \text{ cm}^2$ sheet of kapton. The sheet was copper-clad on both surfaces ($\sim 5 \mu\text{m}$ thick) and chemically etched with a hexagonal array of bi-conical holes of diameter of 50/70 μm (inner/outer), at a pitch of 140 μm . For a thorough review of GEMs, see Ref. [23]. A $7 \times 7 \text{ cm}^2$ cathode was located 1 cm below the GEM stack, defining the detection/drift volume. The cathode was constructed from a $\sim 360 \mu\text{m}$ thick copper mesh with $\sim 500 \mu\text{m}$ pitch. Finally, a 1 mm pitch anode wire grid plane made from 20 μm thick gold plated tungsten wires was situated 3 mm above the top-most GEM (GEM 3), forming the induction gap (further details of this detector can be found in Ref. [18]).

At pressures below 100 Torr we replaced the triple-GEM cascade with THGEMs, which are better suited for high gain operation at low pressures as noted by Ref. [22], and confirmed by our experience here. Even going from 100 Torr to 75 Torr, for example, the maximum stable gas gain in the triple-GEM detector was no longer sufficient to image the electron tracks from ^{55}Fe interactions.¹ All THGEMs used in our studies were fabricated at CERN using a 0.4 mm thick PCB with ~ 0.3 mm holes mechanically drilled in a hexagonal pattern with a pitch of ~ 0.5 mm. To

¹In addition, due to the lower ionization (scintillation) density of the longer tracks at lower pressures, it is not sufficient to simply maintain gas gain.



(a) Detector Vessel



(b) Detection Volume

Figure 1: (a) A simplified drawing of the CCD detector showing the aluminum vacuum vessel and CCD camera setup, excluding the rotary feedthrough, camera mount, and calibration sources for clarity. The light blocking box is also excluded to show the lens and extension tube. (b) A close up view of the detection volume, showing the locations of the calibration sources, cathode, wire grid, and GEMs/THGEMs.

eliminate burring from the drilling process, an annular region of thickness 0.05 mm was chemically etched around each hole.

In our 50 Torr measurements a single THGEM with an active region of $3 \times 3 \text{ cm}^2$ was used. To better accommodate the longer tracks at these low pressures, the drift gap was increased from 1 cm to 2 cm. In addition, the separation from the amplification device and the wire grid was increased from 3 mm to ~ 7 mm, which provided better stability at the lower pressures.

For the 35 Torr measurements a double-THGEM, with a $9.5 \times 9.5 \text{ cm}^2$ active area², was required to achieve the necessary gas gain. The drift gap, transfer gap between the THGEMs, and induction gap between the THGEM and wire grid were 2 cm, 4 mm, and 9.5 mm, respectively. In addition, the wire grid size was increased to match the THGEM area by laying copper tape around the perimeter of the wire frame.

The same double-THGEM setup was also used for the lowest, 25 Torr, pressure measurements except that the transfer and induction gaps were changed to 6.5 mm.

For all measurements, the detector was housed inside a ~ 10 liter cylindrical aluminum vacuum vessel. Calibration was done using internally mounted ^{55}Fe (5.9 keV X-rays) and ^{210}Po (5.3 MeV alphas) sources, which could be individually turned on or off using a rotary feed-through (Figure 1b). Prior to powering on the GEMs/THGEMs, the vacuum vessel was pumped out to $\sim 10^{-3}$ Torr for at least one day before back-filling with high purity (99.999%) CF₄ gas. A 4-inch diameter BK-7 glass window was positioned above the wire grid to allow scintillation light from the final amplification stage to be transmitted to and imaged by the lens and CCD camera. BK-7 glass is a low-cost option to quartz that has a relatively high transmittance ($\geq 90\%$ in the 350-2100 nm range) for the optical component of the CF₄ scintillation, which peaks around 620 nm [24, 25].

The optical system consisted of a fast 58 mm f/1.2 Nikon Noct-NIKKOR lens coupled to a back-illuminated Finger Lakes Instrumentation (FLI) CCD camera (MicroLine ML4710-1-MB) through a 20 mm extension tube for close-focus imaging. The whole setup was mounted on top of the vacuum vessel (Figure 1a) in a light tight box. The camera contained an 18.8 mm diagonal E2V sensor with a 1024×1024 pixel array (CCD47-10-1-353), consisting of $13 \times 13 \mu\text{m}^2$ pixels. The mid-band coated CCD sensor had a peak quantum efficiency of 96% at 560 nm and could be cooled down to a stable operating temperature of -38°C using the built-in Peltier cooler. Two readout speeds were available, 700 kHz and 2 MHz, with 16-bit digitization and a maximum 16×16 on-chip pixel binning. At the lowest operating temperature and slowest readout mode, the read noise was $\sim 10 \text{ e}^- \text{ rms}$ and the dark current was $\sim 0.03 \text{ e}^-/\text{pix/sec}$ with 1×1 on-chip pixel binning. At our focusing distance, the CCD-lens system imaged a $\sim 3 \times 3 \text{ cm}^2$ physical region of the GEM/THGEM surface. The known pitch of the holes on this surface was used to calibrate the length-scale of the images.

3 Detector Calibrations

3.1 GEM/THGEM Gain

The gas gain was determined using an ORTEC 142IH charge sensitive preamplifier to read out the charge signal from the last GEM/THGEM surface. This required calibrating the preamplifier gain

²Two $3 \times 3 \text{ cm}^2$ THGEMs were not available.

Table 1: Experimental configurations

Pressure [Torr]	Gas Gain	E_{Drift} [V/cm]	$\Delta V_{(\text{TH})\text{GEM1}}$ [V]	$\Delta V_{(\text{TH})\text{GEM2}}$ [V]	$\Delta V_{(\text{TH})\text{GEM3}}$ [V]	E_{12} [V/cm]	E_{23} [V/cm]	E_I [V/cm]
100	$\sim 1 \times 10^5$	400	279	334	380	1400	1670	260
100	$\sim 2 \times 10^5$	400	290	290	450	1450	1450	360
50	$\sim 1.5 \times 10^5$	200	830	—	—	—	—	824
35	$\sim 1.6 \times 10^5$	200	573	470	—	718	—	495
25	$\sim 3 \times 10^5$	200	450	650	—	709	—	682

(fC/V) by injecting a known charge and measuring the output voltage. This was done by connecting an ORTEC 448 research pulse generator to the preamplifier via a test input with a built-in 1 pF capacitor, intended for this purpose. The 5.9 keV ^{55}Fe X-ray calibration source was then used to determine the effective gas gain from the output voltage signal of the preamplifier. The conversion of the X-ray created 172 electron-ion pairs on average, which was calculated from the W-value (the average energy per ionization) of 34.2 eV for CF_4 [26].

For each pressure the maximum stable gain was determined iteratively by raising the GEM/THGEM voltages and testing for stability. The latter was done by firing a highly ionizing source (^{210}Po alpha source) into the detection volume. If no sparks occurred over several hours, then the voltage setting was deemed stable and the procedure repeated.

At a pressure of 100 Torr, a maximum stable effective gain of $\sim 1 \times 10^5$ was achieved with the experimental parameters given in Table 1. There, the voltage differences across the GEM electrodes are labeled by ΔV_{GEM1} , ΔV_{GEM2} , and ΔV_{GEM3} , the drift field by E_{Drift} , the transfer field between GEM 1 and 2 by E_{12} , and between GEM 2 and 3 by E_{23} , and the induction field between GEM 3 and the grid by E_I . By raising the GEM voltages (see Table 1) we were able to achieve a higher effective gain of $\sim 2 \times 10^5$. This setting, however, was not entirely stable under alpha irradiation, which initiated a spark about once per hour. Nevertheless, we were able to acquire ^{55}Fe images and an energy spectrum without any sparks at this setting.

For the 50 Torr measurements, 830 V was applied across the THGEM and the drift field was set to 200 V/cm (same E/p as in the 100 Torr measurements). The induction field was 824 V/cm with the wire grid set to a lower voltage than the top THGEM surface so that all electrons produced in the avalanche were collected by this electrode. The experimental parameters are summarized in Table 1. For this measurement we estimate the gain to be $\sim 1.5 \times 10^5$. The stability at this voltage against sparking was similar to that of the highest gain setting at 100 Torr, in that ~ 1 spark/hr was observed when irradiated with alphas. However, unlike for the high gain 100 Torr case, we found an increase in instabilities after data taking commenced at 50 Torr. As a consequence we took only a small sample of ^{55}Fe data (see Section 4.2).

For the 35 Torr and 25 Torr measurements two THGEMs were used with bias voltages and other parameters given in Table 1. At both of these pressures the induction field was oriented as in the 50 Torr measurements, with the wire grid set to a lower voltage than the top THGEM surface so that all electrons produced in the avalanche were collected by the latter electrode. For 35 Torr

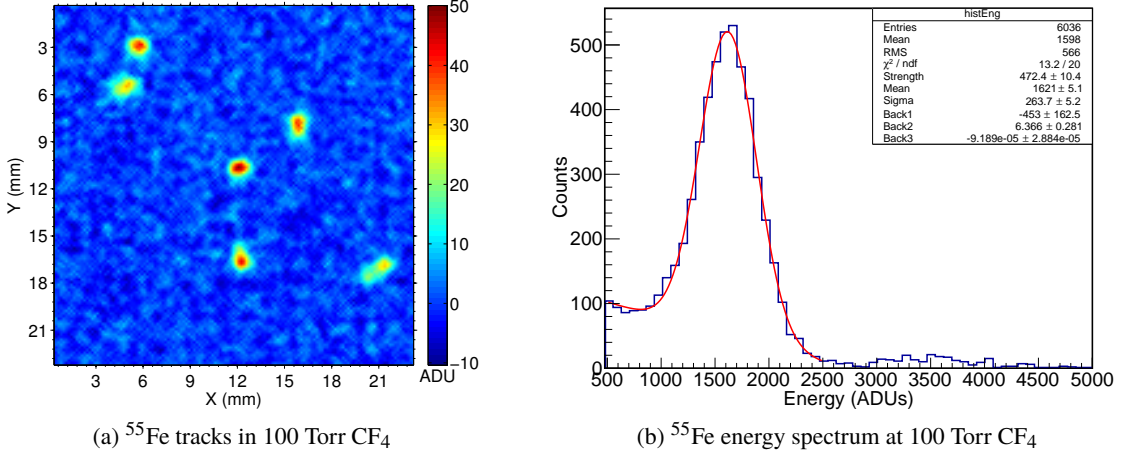


Figure 2: (a) An image of electron tracks from ^{55}Fe X-ray interactions (henceforth referred to as ^{55}Fe tracks) acquired at 6×6 on-chip binning (pixel scale of $165 \mu\text{m}/\text{pix}$) in 100 Torr CF₄ with an averaging filter of block size 5×5 applied to the image to enhance signal-to-noise. The image is captured at the maximum stable gas gain of $\sim 10^5$ and has a pixel scale of $165 \mu\text{m}/\text{pix}$. (b) An energy spectrum of ^{55}Fe obtained optically from CCD imaging of electronic recoil tracks at 6×6 on-chip binning and the maximum stable gain. The data is a combination of the start and end data sets in the day eight run (see Section 4.3 and Figure 8). The smaller secondary feature to the right of the primary peak is the result of event pile-up.

we estimate the gas gain to be $\sim 1.6 \times 10^5$, which was found to be stable throughout data taking. At 25 Torr the gain is estimated to be $\sim 3 \times 10^5$, but due to occasional discharges only a small amount of ^{55}Fe data was taken.

3.2 CCD Calibration

The CCD images (or frames) were calibrated using a set of co-averaged flat-field and dark frames. An exposure time of 5 seconds was chosen for the acquisition of both calibration and data images. Dark frames, taken with the camera shutter closed, were used to correct for the variable accumulation rate of dark current across the pixels in the CCD sensor. Flat-field frames, used to correct for vignetting and pixel to pixel variation in light sensitivity, were acquired by taking exposures of a uniformly illuminated screen. For each type of calibration frame, a set was acquired and co-averaged together to create a master calibration frame. For accuracy, the averaging required rejecting pixels in individual frames that suffered direct hits from cosmic rays or radioactivity. This was done using an algorithm that compared the value of the same pixel across the set of frames, excluding those above three sigmas of the initial average of the pixels. The average was re-computed and the process iterated until there was a convergence in the average value of the pixels. Finally, the data image was calibrated by subtracting the master dark frame and dividing the resulting frame by the normalized, master flat-field frame.

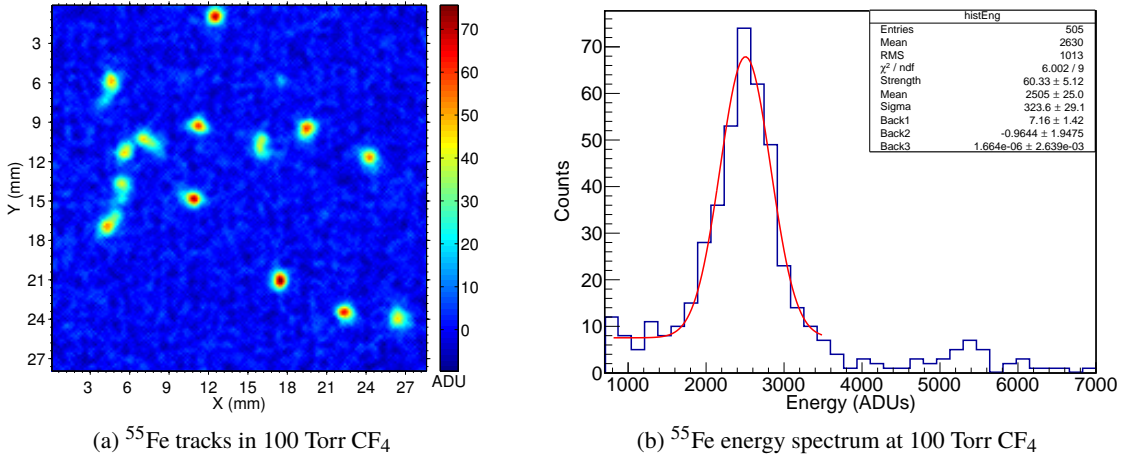


Figure 3: (a) An image of ^{55}Fe tracks acquired at 6×6 on-chip binning in 100 Torr CF₄ with an averaging filter of block size 5×5 applied to the image to enhance signal-to-noise. The image is captured at the maximum gas gain of $\sim 2 \times 10^5$ and shows that even in 100 Torr, ^{55}Fe tracks are resolved. (b) An ^{55}Fe energy spectrum obtained optically from CCD imaging of electronic recoil tracks at 6×6 on-chip binning and maximum gain of $\sim 2 \times 10^5$. The smaller secondary feature to the right of the primary peak is due to event pile-up.

4 Results

4.1 100 Torr

A sample image containing electron tracks from the absorption of ^{55}Fe X-ray (henceforth referred to as ^{55}Fe tracks) taken at the maximum stable gain settings in 100 Torr CF₄ is shown in Figure 2a. On chip binning of 6×6 was used for this image, resulting in each binned pixel imaging 165 μm in real space. The signal is well above the noise in the CCD image and individual tracks are resolved. With this level of signal-to-noise and spatial resolution one could easily characterize the spatial uniformity of gas gain across the GEMs using ^{55}Fe tracks. This provides an attractive alternative to the use of high flux X-ray generators commonly used for quality control of GEMs (e.g. Ref. [27]).

The energy spectrum of the scintillation light from individual ^{55}Fe electron tracks is shown in Figure 2b in units of ADUs³. The peak value in the spectrum is obtained from a fit using a single Gaussian for the signal component, and a constant plus exponential for the background component. The parameters labeled Strength, Mean, and Sigma in the information window of the plot correspond to the Gaussian component, whereas the parameter Back1 belongs to the constant component and the parameters Back2 and Back3 belong to the exponential component. As noted above, the background is the sum of the constant and exponential components. The range of the fit is set so as to exclude the secondary peak seen at ~ 3500 ADU, which is due to pile-up events. The fit has a reduced χ^2 (χ^2 / ndf) = 0.66, a peak value of $\mu = 1621 \pm 5$, and $\sigma = 264 \pm 5$. The FWHM energy resolution is 38% and, setting the peak value from the fit equal to 5.9 keV, we obtain an energy conversion factor of 275 ADUs/keV.

³Analog to Digital Units, with 1 ADU equal to $\sim 1.3 e^-$ produced in our CCD sensor.

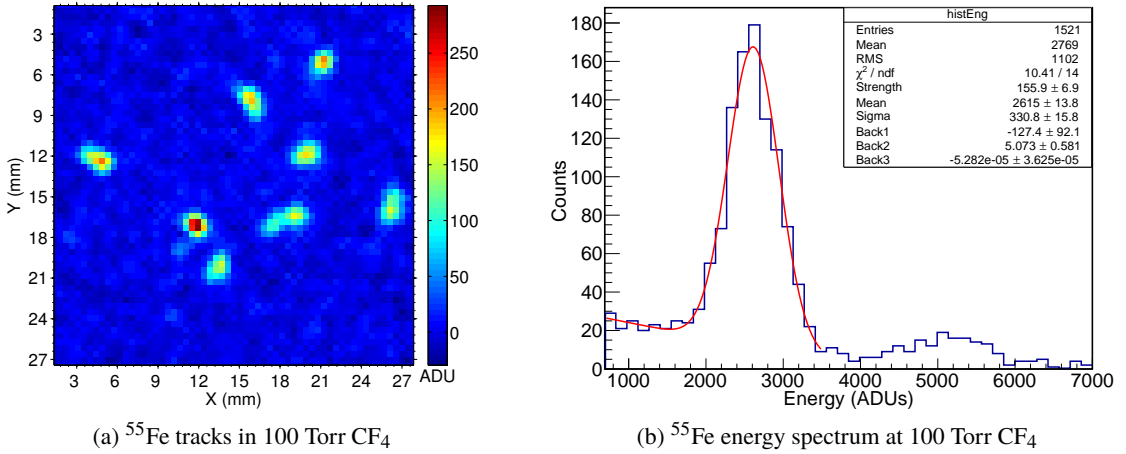


Figure 4: (a) An image of ^{55}Fe tracks acquired at 16×16 on-chip binning (pixel scale of $440 \mu\text{m}/\text{pix}$) in 100 Torr CF_4 with an averaging filter of block size 3×3 applied to the image to enhance signal-to-noise. The image is captured at the maximum gas gain of $\sim 2 \times 10^5$ and shows that even in 100 Torr, low energy 5.9 keV electron tracks are resolved. (b) An ^{55}Fe energy spectrum obtained optically from CCD imaging of electronic recoil tracks at 16×16 on-chip binning and maximum gain of $\sim 2 \times 10^5$. The smaller secondary feature to the right of the primary peak is due to event pile-up.

In Figures 3a and 3b, a sample image of ^{55}Fe tracks in 100 Torr CF_4 at a higher gain ($\sim 2 \times 10^5$), also imaged at 6×6 binning, is shown along with the corresponding energy spectrum. The same procedure for fitting the spectrum as described above gives a peak value $\mu = 2505 \pm 25$, $\sigma = 324 \pm 29$, and energy conversion factor of 425 ADUs/keV. Interestingly, the FWHM energy resolution is 30%, significantly better than that of the moderate gain 100 Torr data at the same image binning.

Data at the high gain setting was also acquired with 16×16 binning, where the contribution from read noise, per real-space area, is lower than 6×6 binning. A sample image of ^{55}Fe tracks at this binning and the corresponding energy spectrum are shown in Figures 4a and 4b. A fit to the latter gave $\mu = 2615 \pm 14$, $\sigma = 331 \pm 16$, and an energy conversion factor of 443 ADUs/keV. Although the FWHM energy resolution of both the 16×16 and 6×6 binned data was 30%, the former binning resulted in a 4% higher peak. This could be due to the higher signal-to-noise with 16×16 binning, resulting in better efficiency for finding the entire track. However, we cannot rule out the possibility of a drift in gas gain over the time taken between acquiring the two data sets.

4.2 25, 35 & 50 Torr

In Figure 5, two sample images of ^{55}Fe tracks taken using a single THGEM at a pressure of 50 Torr in CF_4 are shown. As expected, the tracks are longer and much better resolved than those in the 100 Torr data and, in addition, ionization density gradients along the electron tracks are also clearly visible. In a number of tracks a clear assymmetry in ionization density is seen, which allows one to reconstruct the start (low density) and end (high density) of the electron track. The corresponding energy spectrum is not shown due to an increase in electrical instabilities, as stated in Section 3.1. Instead of risking damage to the THGEM we took just a small amount of data in this

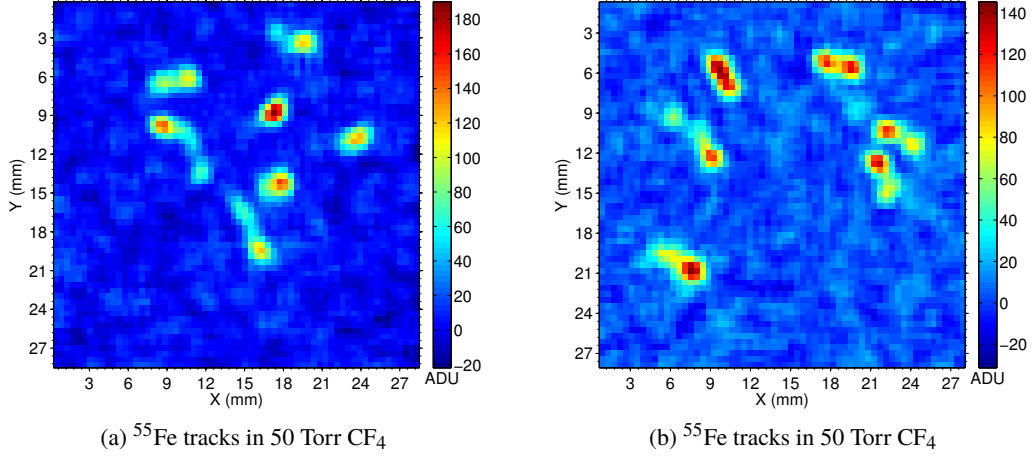


Figure 5: (a)-(b) Images of ^{55}Fe tracks in 50 Torr CF₄ at 16×16 on-chip binning. An averaging filter with a 3×3 block size has been applied to the image to improve signal-to-noise without significantly degrading resolution. At this pressure, the tracks are well resolved and fluctuations in energy loss and range straggling are also clearly observable.

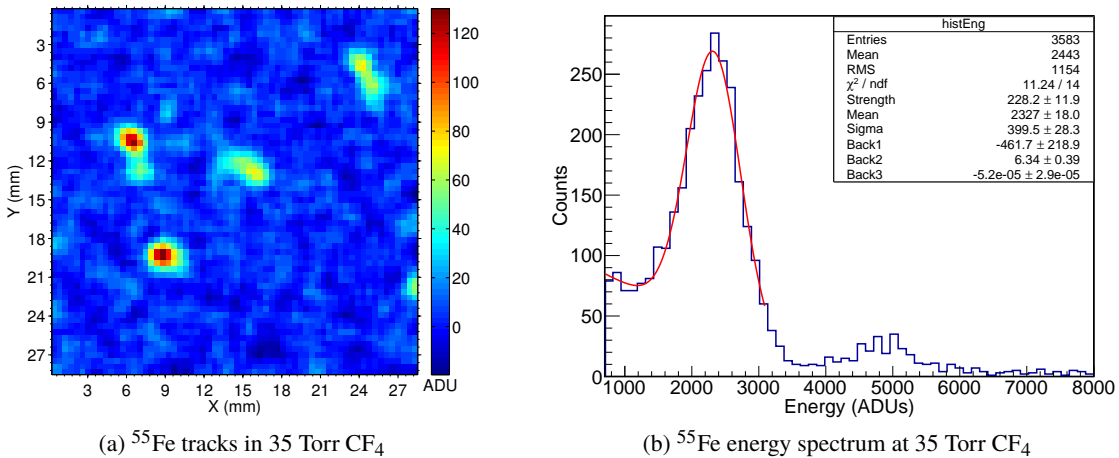


Figure 6: (a) An image of ^{55}Fe tracks in 35 Torr CF₄ with an averaging filter applied to enhance signal to noise. The tracks are clearly resolvable as extended objects rather than diffused points at this pressure. (b) An energy spectrum obtained from CCD imaged ^{55}Fe electronic recoil tracks in 35 Torr at 16×16 on-chip binning and maximum stable gain. The smaller secondary feature on the right of the primary peak is due to event pile-up.

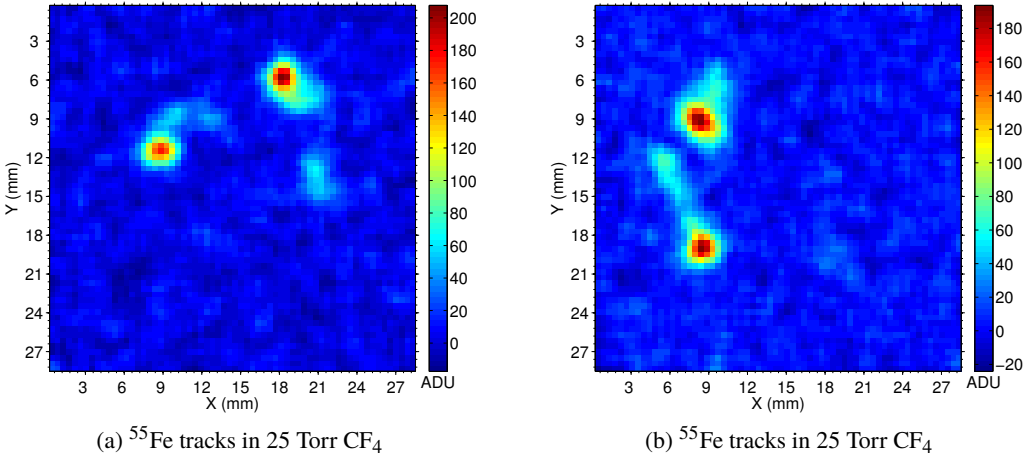


Figure 7: (a)-(b) Sample images of ^{55}Fe tracks in 25 Torr CF₄ using two THGEMs and 16×16 CCD on-chip binning. A 5×5 averaging filter has been applied to enhance signal to noise. The tracks are resolvable at this pressure and gas gain.

configuration. Nevertheless, as the images in Figure 5 unambiguously show, TPCs with CCD-based optical readouts and sufficiently high signal-to-noise and imaging resolution, can *resolve* electron tracks with energies as low as 5.9 keV.

For the 35 Torr CF₄ measurements 2 THGEMs were required to obtain sufficient gas gain (see Section 2 and Table 1). Figure 6a shows a sample image containing ^{55}Fe tracks taken in this configuration. The energy spectrum obtained from a series of these images is shown in Figure 6b. A fit of the spectrum using the same functions for signal and background as for the 100 Torr data (Section 4.1) gives a reduced χ^2 (χ^2/ndf) = 0.80. The fitted peak value is $\mu = 2327 \pm 18$ and $\sigma = 400 \pm 28$. This gives a FWHM energy resolution of 40% which is similar to, within errors, the energy resolution obtained from the moderate gain 100 Torr data.

As in the 50 Torr data the tracks in 35 Torr are clearly resolved but the resolution is poorer due to the presence of the second THGEM and the transfer region within the double THGEM amplification structure. This is expected and is due to two effects. The first is that the holes of the 2 THGEMs are not aligned, so that the charge cloud forming the track will suffer broadening as it passes from THGEM 1 to THGEM 2. For the larger hole pitch, ~ 0.4 mm, of THGEMs (relative to thin GEMs) this could be a significant effect. The second effect is due to the additional diffusion of the charge cloud as it traverses the 4 mm transfer gap. This diffusion is worse, per unit drift length, than in the drift region because the transfer E field is so high. Using MAGBOLTZ [28] we estimate that the transverse diffusion in the 0.4 cm transfer gap is $\sigma = 545 \mu\text{m}$, compared to $\sigma = 465 \mu\text{m}$ in the 2 cm drift region.

Finally, in Figure 7 we present sample images of ^{55}Fe tracks acquired in 25 Torr CF₄. However, there was insufficient data taken for an energy spectrum because electrical instabilities (discharges) prevented a long data run. But with additional fine tuning of THGEM voltages and the detector setup, it is conceivable that stable operation could be achieved at the necessary gas gains needed to image individual ^{55}Fe tracks.

Table 2: Summary of Results

Pressure [Torr]	Amplification Stage	Gas Gain	Pixel Binning	FWHM Energy Resolution [%]	Energy Conversion Factor [ADU/keV]	Average Track Length [mm]
100	3-GEMs	$\sim 1 \times 10^5$	6×6	38	275	1.9
100	3-GEMs	$\sim 2 \times 10^5$	6×6	30	425	2.0
100	3-GEMs	$\sim 2 \times 10^5$	16×16	30	443	2.5
50	1-THGEM	$\sim 1.5 \times 10^5$	16×16	–	–	~ 3.7
35	2-THGEMs	$\sim 1.6 \times 10^5$	16×16	40	394	4.1
25	2-THGEMs	$> 2 \times 10^5$	16×16	–	–	~ 4.6

A summary of the results for the different data sets and their corresponding detector configurations is found in Table 2. In addition to the parameters previously discussed, the average ^{55}Fe track length for each detector configuration is also included. We note that this quantity is the detected track length, which depends on multiple factors besides the gas pressure. These include diffusion, smearing within the amplification stage, gas gain (signal-to-noise), and CCD pixel binning. Thus, the track length does not simply scale with pressure in the measurements shown in the Table.

4.3 Light Yield and Contaminants

Two effects on the light yield in 100 Torr CF_4 were observed in our ^{55}Fe data when acquired over many days. The first was due to contamination from out-gassing, and the second was the possible indication of light quenching at high gas gains. We discuss these here.

^{55}Fe calibrations were required over 8 days for a different application⁴, providing us data to study the effects of possible gas contaminants on the light yield. Before the start of the 8 day data run, the detector vessel was sealed and pumped out to $\sim 10^{-3}$ Torr overnight. Subsequently, each day of data taking started by back-filling the detector vessel to 100 Torr with 99.999% pure CF_4 , powering up the detector and acquiring ~ 70 minutes of ^{55}Fe data. This was followed by ~ 14 hours of neutron data and a second ~ 70 minute ^{55}Fe exposure at the end of the day, after which the detector was powered down and the vessel pumped out for ~ 3 hours. This procedure was repeated for each day of data taking. The GEMs were powered up to the same voltages each day, with the values given in Section 3.1 and Table 1 for the moderate, stable gas gain of $\sim 1 \times 10^5$. The ^{55}Fe spectrum obtained from the charge signal was used to monitor the gas gain, which remained constant within 10% over the 8 days. The ^{55}Fe spectrum obtained from the optical signal over this period, however, showed an increase in the light yield, which is highly sensitive to gas purity (e.g., [29]). With the detector kept sealed over the 8 days, out-gassing would be the main source of contamination with the expectation that its rate would decrease over time.

The results of the data runs are plotted in Figure 8, which shows the fitted peak value of the optical ^{55}Fe spectrum at the start and end of each of the 8 days of data acquisition. The large

⁴These were acquired for calibration of neutron exposures of the detector for directional studies.

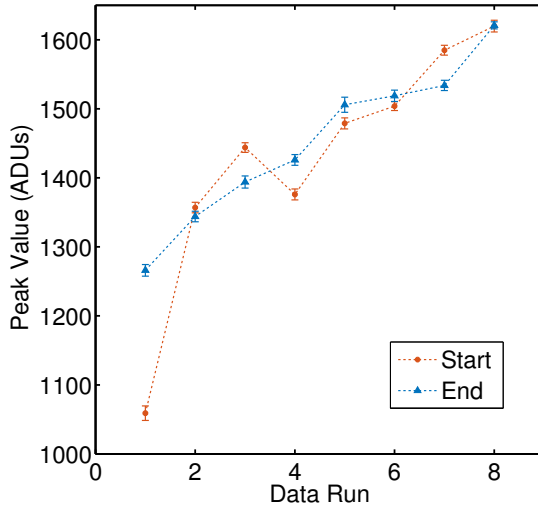


Figure 8: The fitted peak value of the ^{55}Fe energy spectrum at the start and end of the day over eight days of data taking. With the exception of the first data run, the start and end peak values are within 4%. The large change ($\sim 20\%$) seen between the start and end in the first data set is likely due to insufficient time for the GEMs to charge up and stabilize. The raising peak value with run number is likely the result of a reduction in concentration of contaminants with the additional pump down in-between runs.

difference in the start and end spectrum peak values for data run 1 is most likely the result of insufficient time given between GEM power up and data taking; we discovered that the GEMs required about 1-2 hours after being brought up to voltage before stable operation ensued.

With the exception of run 1, the start and end spectrum peak values are always within 4% of each other, which suggests that any compositional change of the gas does not affect the light output significantly over a single day. However, over 8 days the curves in Figure 8 show a gradual rise in the light output. Between run 2 and run 8 the light output increased by 21% in the end series, and by 19% in the start series. The light yield in the end series is monotonically increasing whereas that in the start series has more scatter. This is due to the variability in the time between GEM power up and data taking, as discussed above. Nevertheless, the steady increase in light yield over the 8 days is consistent with improved gas purity. We attribute this to a decrease in the out-gassing rate, which can have a long half-life in sealed vessels that have not been baked out.

The second effect, possibly due to light quenching, was the change in the ratio of the optical ^{55}Fe spectrum peak and the corresponding effective gas gain for the two gain settings, $\sim 1 \times 10^5$ and $\sim 2 \times 10^5$. In the lower gain data, this ratio was ~ 0.016 , and in the high gain data it was ~ 0.013 . This ratio, which can be thought of as an effective photon yield (photons per secondary electron), is lower by $\sim 19\%$ at the higher gas gain. Unfortunately, the low and high gain measurements were taken months apart so it is difficult to definitively attribute the lower photon yield to quenching. We nevertheless describe the various possibilities that could cause the lower light yield as some of them have important implications for applications such as directional dark matter searches.

The simplest explanation for the observed differences in light yield is that there were more

contaminants due to out-gassing in the high gain measurements. Given that the high and low gas gain measurements were taken several months apart under different conditions, we cannot rule out this possibility.

The second possibility is that it could be a charge density effect, where the photon yield decreases (is quenched) as the charge density increases at high gas gains. This quenching could be either due to a reduction in total light yield, or just over the wavelength range of sensitivity for our CCD camera and lens due to a change in the emission spectrum of CF_4 .

Quenching due to high charge density arising from either high gas gains and/or high primary ionization densities has important consequences for applications where measuring the charge density along a recoil track is required. An example is directional dark matter detection in which the sense (vector direction) of the ionization track is determined by measuring the asymmetry in the charge deposition along the track. If quenching plays a significant role in the low pressure regime where directional dark matter experiments operate, it could limit how well the directional signature can be measured in gas based TPCs operated at high gas gains.

5 Conclusion

We have shown that a GEM and THGEM based TPC detector can be operated in low pressure CF_4 (25-100 Torr) with effective gas gains exceeding 2×10^5 . With the high signal-to-noise and spatial resolution of this detector, it was possible to image and resolve individual ^{55}Fe tracks using an optical readout consisting of a fast lens and a low noise CCD camera. ^{55}Fe spectra were derived using the optical signal from these tracks, demonstrating good energy resolution with FWHM down to $\sim 30\%$. These results show that low pressure gas TPCs with optical readout could provide an interesting alternative to, and potential advantages over, traditional charge readout. Specific areas that could benefit from this work are X-ray polarimetry and directional dark matter detection experiments, both requiring detailed track reconstruction of ionizing particles down to the lowest energies.

Acknowledgements

This material is based upon work supported by the NSF under Grant Nos. 0548208, 1103420, and 1407773.

References

- [1] R. Bellazzini, G. Spandre, N. Lumb, Nucl. Instr. Meth. 478 (2002) 13-25.
- [2] E. Costa, P. Soffitta, R. Bellazzini, A. Brez, N. Lumb, and G. Spandre, Nature 411 (2001) 662-665.
- [3] J. K. Black, P. Deines-Jones, S. E. Ready, R. A. Street, Nucl. Instr. Meth. Phys. Res. A 513 (2003) 639-643.
- [4] J. K. Black, R.G. Baker, P. Deines-Jones, J.E. Hill, K. Jahoda, Nucl. Instr. Meth. Phys. Res. A 581 (2007) 755-760.
- [5] H. Sakurai, et al., Nucl. Instr. Meth. Phys. Res. A 505 (2003) 219-222.

- [6] H. Sakurai, et al., Nucl. Instr. Meth. Phys. Res. A 513 (2003) 282-286.
- [7] H. Sakurai, et al., Nucl. Instr. Meth. Phys. Res. A 525 (2004) 6-11.
- [8] D. N. Spergel, Phys. Rev. D37 (1998) 1353-1355.
- [9] K. N. Buckland, M. J. Lehner, G. E. Masek, and M. Mojaver, Phys. Rev. Lett. 73 (1994) 1067-1070.
- [10] D. P. Snowden-Ifft, T. Ohnuki, E. S. Rykoff, C. J. Martoff, Nucl. Instr. Meth. A 498 (2003) 155-164.
- [11] S. Burgos, et al., Astropart. Phys. 31 (2009) 261-266.
- [12] S. Burgos, et al., Nucl. Instr. Meth. A 600 (2009) 417-423
- [13] L. M. S. Margato, et al., Nucl. Instr. Meth. Phys. Res. A 504 (2003) 374-378.
- [14] L. M. S. Margato, et al., Nucl. Instr. Meth. Phys. Res. A 535 (2004) 231-235.
- [15] R. A. Austin and B. D. Ramsey, Optical Engineering 32 (1993) 1990-1995.
- [16] F. A. F. Fraga, et al., Nucl. Instr. Meth. Phys. Res. A 471 (2001) 125-130.
- [17] D. Dujmic, et al., Astropart. Phys. 30 (2008) 58?64.
- [18] N. S. Phan, R. J. Lauer, E. R. Lee, D. Loomba, J. A. J. Matthews, E. H. Miller, Astropart. Phys. 84 (2016) 82-96.
- [19] F. Sauli, Nucl. Instr. and Meth. Phys. Res. A 386 (1997) 531-534.
- [20] F. A. F. Fraga, et al., Nucl. Instr. and Meth. Phys. Res. A 478 (2002) 357-361.
- [21] F. A. F. Fraga, et al., Nucl. Instr. and Meth. Phys. Res. A 513 (2003) 379-387.
- [22] C. K. Shalem, R. Chechik, A. Breskin, K. Michaeli, N. Ben-Haim, Nucl. Instr. Meth. Phys. Res. A 558 (2006) 468-474.
- [23] A. F. Buzulutskov, Instr. Exp. Tech., 2007, Vol. 50, No. 3, pp. 287.
- [24] A. Morozov, et al., Nucl. Instr. Meth. Phys. Res. B 268 (2010) 1456-1459.
- [25] A. Kaboth, et al., Nucl. Instr. and Meth. Phys. Res. A 592 (2008) 63-72.
- [26] G. F. Reinking, L. G. Christopoulo, S. R. Hunter, J. Appl. Phys. 60, 499 (1986).
- [27] F. A. F. Fraga, S. T. G. Fetal, R. Ferreira Marques, A. J. P. L. Policarpo, Nucl. Instr. Meth. Phys. Res. A 442 (2000) 417-422.
- [28] S. Biagi, Nucl. Instr. Meth. Phys. Res. A 421 (1-2) (1999) 234â\\$240.
- [29] L. M. S. Margato, et al., Nucl. Instr. Meth. Phys. Res. A, 695 (2012), p. 425.